Forging Fast Ion Conducting Nanochannels with Swift Heavy Ions: The Correlated Role of Local Electronic and Atomic structure

Ritesh Sachan[1], Valentino R. Cooper[1], Bin Liu[2], Dilpuneet S. Aidhy[3], Brian K. Voas[4], Maik Lang[5], Xin Ou[6], Christina Trautmann[7,8], Yanwen Zhang[1,2], Matthew F. Chisholm[1], and William J. Weber[2,1]*

[1]Material Science and Technology Division, Oak Ridge National Laboratory, Oak Ridge, TN, 37831, USA
[2]Department of Materials Science and Engineering, University of Tennessee, Knoxville, TN, 37996, USA
[3]Department of Mechanical Engineering, University of Wyoming, Laramie, WY, 82071, USA
[4]Department of Materials Science and Engineering, Iowa State University, Ames, Iowa, 50011, USA
[5]Department of Nuclear Engineering, University of Tennessee, Knoxville, TN, 37996, USA
[6]State Key Laboratory of Functional Material for Informatics, Chinese Academy of Sciences, Shanghai, 200050, China
[7]GSI Helmholtzzentrum für Schwerionenforschung GmbH, Planckstrasse, 1, D-64291, Darmstadt, Germany
[8]Materialwissenschaft, Technische Universität Darmstadt, Darmstadt, 64287, Germany
*email:sachanr@ornl.gov

ABSTRACT

Atomically disordered oxides have attracted significant attention in recent years due to the possibility of enhanced ionic conductivity. However, the correlation between atomic disorder, corresponding electronic structure and the resulting oxygen diffusivity is not well understood. The disordered variants of the ordered pyrochlore structure in gadolinium titanate ($Gd_2Ti_2O_7$) are seen as a particularly interesting prospect due to intrinsic presence of a vacant oxygen site in the unit atomic structure which could provide channel for fast oxygen conduction. In the present work, we provide the insights at sub-angstrom scale on the disordering induced variations in the local atomic environment and its effect on the electronic structure in high energy ion irradiation induced disordered nanochannels, which can be utilized as pathways for fast oxygen ion transport. With the help of an atomic plane-by-plane resolved analyses, the work shows how the presence of various types of TiO_x polyhedral that exist in the amorphous and disordered crystalline phase modify the electronic structures relative to the ordered pyrochlore phase in $Gd_2Ti_2O_7$. The correlated molecular dynamics simulations on the disordered structures show a remarkable enhancement in oxygen diffusivity as compared to ordered pyrochlore lattice and make that a suitable candidate for applications requiring fast oxygen conduction.

INTRODUCTION

Presently, a prime focus in materials research is on the understanding of the atomic structure in fast ion conducting complex oxides for improved energy storage and conversion. It has been shown that disordered phases in complex oxides lead to higher oxygen mobility and conductivity due to the lack of distinct arrangement of lattice sites between different cations in contrast to the ordered structures.[1-3] A variety of disordered oxides, including disordered crystalline, amorphous and heavily doped defective structures, are reported to exhibit fast ionic conduction.[3-7] Among these, disordered phases derived from pyrochlore oxides ($A_2B_2O_7$) are seen as well-suited candidates due to its atomic arrangement and the nature of their fast oxygen ion transport.[6-9] Pyrochlore structured oxides, in general, are interesting due to presence of one vacant site per eight oxygen sites which can provide fast diffusion of oxygen ions.[10,11] The disordering of the atomic arrangement, in which cations occupy A and B sites randomly and the oxygen anion sites become indistinguishable, dramatically increases the mobility of oxygen ions, comparable to or higher than yttria-stabilized zirconia.[12] The importance of the structural disordering is not only observed in energy storage and conversion applications, but also demonstrated an improvement in both catalytic activity and radiation resistance.[13-18] However, a major obstacle in this area is the limited understanding of disordered phases at the atomic scale in terms of both atomic and electronic structure characteristics.

Few studies have been performed by X-ray absorption near structure (XANES) spectroscopy and neutron scattering materials which shed light on the electronic structure of bulk phases in various $A_2B_2O_7$ compounds.[19-21] The inter-relationships of various aspects of materials' properties, such as phase formation, composition, structural distortions and consequential changes in electronic structure due to energetic ion irradiation have not been examined.

In this work, with the help of plane-by-plane resolved fine structure analysis by electron energy-loss spectroscopy (EELS) in a scanning transmission electron microscopy (STEM) and correlative density functional theory (DFT), we provide insights on the correlation of electronic structure with the atomic arrangement in $Gd_2Ti_2O_7$. The work demonstrates how the presence of various types of TiO_x polyhedral that exist in the amorphous and disordered crystalline phase play a critical role in modifying the electronic structures as compared to the ordered pyrochlore phase in $Gd_2Ti_2O_7$. We also estimated the enhancement in oxygen conductivity through the mean square displacement simulations on the studied disordered structures on $Gd_2Ti_xZr_{2-x}O_7$ (x = 0, 1 and 2) to propose an application in fast oxygen transport.

EXPERIMENTAL AND COMPUTATIONAL METHODS

Ion irradiation. The polycrystalline $Gd_2Ti_2O_7$ samples were prepared by the sol-gel method, followed by a sintering process at 1875 K for 50 hrs in air. There were two sets of samples used in the experiment, (a) ~40 μm and (b) ~1 mm thick. The samples for 2.2 GeV Au energy irradiation were polished down to ~ 40 μm thickness to ensure that irradiated ions will pass through the material. The samples irradiated by 55 MeV I were 1 mm thick. The sample (a) and (b) were irradiated by swift heavy 2.2 GeV Au and 55 MeV I ions respectively, using UNILAC linear accelerator in the GSI Helmoltz Center for Heavy Ion Research in Darmstadt, and the Helmholtz-Zentrum Dresden-Rossendorf in Dresden, Germany. For creating isolated ion tracks, the fluence was kept at $5x10^{10}$ ions/cm^2.

STEM Characterization: HAADF imaging was performed on various samples in a 5th order aberration corrected scanning transmission electron microscope (Nion UltraSTEM200) operating at 200 KV. HAADF imaging was done using an inner semi-angle of 65 mrad. The electron probe current used in the experiment was 28±2 pA. The EELS data was acquired with the collection angle of 48 mrad. The fine structure EELS data was collected with 0.1 eV/channel energy

dispersion and 0.04 nm spatial pixel size on the selected area of interest, while, for the elemental mapping, it is collected with 0.5 eV/channel energy dispersion and 0.27 nm spatial pixel size. The samples for STEM analysis were prepared by conventional mechanical thinning, precision polishing and ion-milling in liquid N_2 environment as described in detail in Ref. [11, 22].

Computational: The VASP (Vienna Ab-Initio Simulation Package) code using the projector augmented wave method is used in the present density functional theory (DFT) calculations.[23] The generalized gradient approximation with the exchange correlation potential of Perdew– Burke– Ernzerhof (GGA-PBE) is selected.[24] A 4x4x4 k-point sampling in reciprocal space and a cutoff energy of 450 eV for the plane wave basis set are adopted. The crystal structures are relaxed until the forces on individual atoms are smaller than 0.01 eV/Å.

MD simulations are performed using the large-scale atomic/molecular massively parallel simulator (LAMMPS) code. The Buckingham type interatomic potential form is used, and the potential parameters are taken from the work by Pirzada et al.[10] A 297 atoms structure obtained from SQS structure is used as the input structure for obtaining the high-temperature amorphous structure. A time step of 1 fs is used, and the long-range electrostatic interactions are evaluated using the Ewald summation as modeled in the LAMMPS code, using a cut of 11 Å. Periodic boundary conditions are applied in all directions.

RESULTS AND DISCUSSION

Thermodynamically stable disordered phases, i.e. disordered crystalline (defect fluorite) and amorphous phase, were created through single event high energy ion irradiation on $Gd_2Ti_2O_7$ resulting in individual disordered nanosized channels embedded within the ordered pyrochlore matrix. These nanochannels, also known as ion tracks in the radiation physics community, are atomically disordered cylindrical channels, produced from inelastic interactions of an energetic

ion (MeV to GeV) with the material at extremely short timescales (~100 ps).[25,26] These channels can be potentially used as nanoscale pathways for selective transport of oxygen ions.[9,27] Figure 1a shows an example of such a channel/track embedded in $Gd_2Ti_2O_7$. The magnified cross-sectional image of an individual ion track (Figure 1b) illustrates the morphological uniformity continuity of these channels.

Figure 2 provides quantitative phase identification using high angle annular dark field (HAADF) images of ion tracks created by different energetic ions in $Gd_2Ti_2O_7$ and Gd_2TiZrO_7 matrices. Figure 2a and Figure 2d-2f correspond to tracks created in $Gd_2Ti_2O_7$ by 2.2 GeV Au and 55 MeV I, respectively, while Figure 2c shows the track formed by 2.3 GeV Pb in Gd_2TiZrO_7 matrix. Due to the irradiation of high-energy ions, cylindrical tracks with amorphous core are formed. Based on several acquired HAADF images, the average diameter of tracks formed by 2.2 GeV Au ions and by 55 MeV I ions in $Gd_2Ti_2O_7$ are estimated to be ~7.5±1.0 nm and ~3.5±1.0 nm respectively, and 6.0±2.0 nm in Gd_2TiZrO_7 samples. Since the atomic column intensity in the HAADF image is a measure to identify different phases or atomic arrangements, an intensity profile analysis along several atomic planes was performed. The analysis indicates the presence of a distinct phase with a thickness of 2-3 atomic planes between the ordered crystalline pyrochlore matrix and the amorphous phase in $Gd_2Ti_2O_7$ as demonstrated in Figure 2a, 2e and 2f. This phase is identified as a disordered crystalline defect fluorite structure having a random arrangement of Gd and Ti atoms in cation sites.[3,10,11] A detailed intensity profile analysis, performed along atomic planes starting from theordered pyrochlore matrix (plane 1) to amorphous track core (plane 5), is shown in Figure 2b. The profiles illustrate that the atomic columns with defect fluorite structure appear in plane 3, 4 and 5 (indicated by yellow boxes) forming a ring around the amorphous phase. To validate the analysis method, it is performed on the track formed in Gd_2TiZrO_7 where a thicker (5-7 atomic

plane) defect-fluorite ring is identified. These results show that a concentric disordered defect fluorite phase region with a constant thickness of ~2-3 atomic planes (3-7 Å depending on specific planes) consistently forms around the amorphous phase irrespective of irradiation conditions, which just affect the size of ion tracks. It is important to note that the thickness of the defect fluorite phase obtained from the HAADF image analysis is thinner than previously reported 2±1 nm based on HRTEM image analysis. In the latter, however, phase and Fresnel contrast could interfere with the thickness determination.[28]

As ion track formation consists of highly non-equilibrium melting and cooling events within nanosecond timescale, there is a possibility of localized compositional changes in an ion track. To investigate this possibility, compositional analyses by EELS were performed over an area covering a region from the ordered matrix to the disordered ion track as shown in Figure 3. From the compositional map, it is evident that the average content of Gd, Ti and O remains constant throughout the analyzed region. The median percent composition in the selected region shown in Figure 3a is measured to be 19±2%, 20±2% and 61±2% respectively for Gd, Ti and O. The deviations in composition are within the limits of quantification by EELS.

After accurately determining the width of disordered phases as well as the stoichiometric consistency of the ion tracks, a detailed plane by plane energy-loss near edge structure (ELNES) analysis of Ti $L_{2,3}$-edge (456 eV) and O K-edge (532 eV) by EELS spectra was performed on an ion track as shown in Figure 4, which consists of different planes of the ordered pyrochlore (planes 1-2), defect fluorite (planes 3-4) and amorphous phases (planes 5-7). Figure 4c shows the background subtracted Ti $L_{2,3}$-edge spectra corresponding to planes 1 to 7 of Figure 4b. There are two key conclusions that can be drawn from this figure. First, crystal field splitting exists for all three forms of $Gd_2Ti_2O_7$ that indicates short range ordering of Ti-O bonding persisting even in the

amorphous phase. This is consistent with the previous structural data that showed local order in the defect-fluorite phase.[20] Second, an energy shift in the Ti $L_{2,3}$-edge character is observed between the ordered pyrochlore and the disordered defect-fluorite structures, whereas its character remains largely unchanged between the disordered defect fluorite and the amorphous phase of $Gd_2Ti_2O_7$. The only difference observed between the Ti EEL spectra of disordered defect-fluorite and amorphous phase is slightly more peak broadening in the amorphous structure as compared to defect-fluorite. To examine the transitions in fine structure, a Gaussian peak fitting routine is performed on the Ti L_{23}-edge for all spectra from plane 1 to 7. A representative spectrum with fitted peaks is presented in the supplemental information. A plane-by-plane determination of the fitted peak positions are shown in Figure 4d. It is observed that the shift in the energy positions of peak 2 and 4 towards peak 1 and 3, respectively, take place between plane 2 and 3 (i.e. between the ordered pyrochlore and disordered defect fluorite structures). It should be noted that the peaks of Ti L_{23} are represented with numbers (i.e. Peak 1-4), not with d-orbital labels. The assignment of the t_{2g} and e_g levels in disordered crystalline and amorphous phases is no longer valid. To further confirm these results, similar ELNES analyses were performed on the Gd_2TiZrO_7 sample (Figure 4e) where the ion tracks consist of a thicker defect-fluorite region. As anticipated, we observe that the Ti-L_{23} spectra corresponding to the ordered matrix (R1), disordered defect-fluorite (R2) and amorphous (R3) are consistent with those in $Gd_2Ti_2O_7$ (Figure 4f). Additionally, O-K edge spectra for the same regions in Gd_2TiZrO_7, presented in Figure 4g, exhibit a clear existence of a pre-peak in the ordered pyrochlore that merges with the main peak in the disordered defect fluorite as well as in the amorphous phase. This suggests an overlapping of energy bands due to structural disordering. Overall, these results indicate that, in spite of the difference in crystallinity, the

electronic structure characteristics of the disordered defect fluorite and amorphous structures formed in an ion track are quite similar.

These changes in electronic structure observed in the Ti L_{23} and O K EEL spectra are fingerprints of the variations in Ti local environment that result from (i) changes in Ti-O coordination number and/or (ii) distortions in Ti-O polyhedra. To correlate these changes, we explored the electronic structure of $Gd_2Ti_2O_7$ in ordered pyrochlore (Figure 5a), disordered crystalline (defect fluorite) (Figure 5b) and amorphous phases (Figure 5c) using first-principles DFT calculations. The approach is similar to the one adopted by B. Liu et al.[29] For the pyrochlore phase, the structure is obtained by fully optimizing the standard pyrochlore structure. To simulate the disorder in the defect fluorite structure, the special quasirandom structure (SQS)[30] approach was employed to generate a random arrangement of cations and oxygen vacancies within the fluorite framework as previously done for perovskites[31]. To generate a representative amorphous structure, molecular dynamics simulations of an initial defect fluorite structure were performed at 4000 K. The high temperature structure was then quenched to 0 K. For all phases, the final structures were subsequently fully relaxed with respect to atomic positions and lattice constants within DFT. The detailed atomic configurations of each structure, presented in the supporting information, show the disappearance of long range ordering in the amorphous structure. As illustrated in Figure 5, the pyrochlore structure is well ordered with only corner-sharing, octahedrally coordinated Ti-O polyhedra. Conversely, the defect fluorite and amorphous phases contain Ti with coordination numbers from 6 to 8 as well as with distorted polyhedral (See Figure 5i). The large variations in polyhedral type is visually emphasized in Figure 5, where it is evident that the amorphous phase consists of a higher degree of disorder in comparison with the defect-fluorite and pyrochlore phase. This degree of local disorder can be further quantified through a detailed analysis of the Ti-O local

bonding. Figure 5g and 5h depict histograms of the bond angle deviations (A_i) from the octahedral and fluorite environment as determined with the following equation:

$$A_i = \sum_{m}^{N-1} \sum_{n=m-1}^{N} \cos\left(2 * \left(\Delta\theta_{m,n}\right)\right) \quad (1)$$

where N is the number of nearest neighbor oxygen ions and $\Delta\theta_{m,n}$ is the difference between the O_m-Ti-O_n bond angle and the expected bond angle for an octahedral (90°) or fluorite environment (70.5° or 109.5°). These are tabulated for bond lengths less than 2.8 Å that is roughly 20% larger than the longest possible Ti-O bond, as dictated by the ionic Shannon radii. As anticipated, the bond angle and the coordination number in the pyrochlore structure show very little deviations from that expected of octahderal coordination. On the other hand, significant deviations from octahedral coordination are observed for both the defect fluorite and amorphous structures, suggesting presence of highly distorted and differently coordinated TiO_x polyhedra. In addition, the crystallographic periodicity in the bond angles with certain values is also evident in the defect-fluorite phase while the amorphous phase shows a wider variation, suggesting more randomness in the amorphous atomic configuration (Figure 5g and 5h). Furthermore, Figure 5i shows that the defect fluorite structure has a range of Ti-O coordination numbers with a uniform spread from 6-8 while the majority of the amorphous structure coordination numbers are 7 or 8.

Using these atomic configurations, the density of states (DOS) for Ti were obtained from DFT. The total DOS for Ti for the conduction bands (> 0 eV) for the three phases are depicted in Figure 5d-5f). These states are indirectly correlated to EEL spectra. DOS corresponding to the Ti *d*-states for the pyrochlore structure exhibit two distinct peaks; most likely indicating a separation between the t_{2g} and e_g states that arise from the octahedral splitting in the pyrochlore local environment. Interestingly, we observe a closing of this splitting for the defect fluorite structure. These peaks are significantly broadened relative to the pyrochlore and experimental spectra. Further broadening

is observed for the amorphous structure. The DFT calculations are consistent with the experimental EELS results, which show that the electronic properties of the amorphous phase are similar to the defect fluorite phase due to multiple Ti-O polyhedral types in spite of a loss of crystallinity.

One fact to consider in the study is that, although the experimental EELS data for defect fluorite shows substantial peak broadening and shifts similar to the amorphous phase, it still exhibits splitting reminiscent of the octahedral crystal field splitting in the pyrochlore structure. On the contrary, we see that Ti *d*-states DOS obtained from DFT calculations for the defect fluorite structure, have a continuum of DOS as compared to discrete energy levels expected from the EELS. A careful analysis of this structure indicates that some of the sites have octahedral-like environments. This suggests that, in the case of the experimental defect phases, it is likely that these octahedral-like sites dominate the spectra of the defect fluorite phases. Our bond-angle and bond-order analyses show a mix of oxygen coordination which would affect the splitting. A possible reason is the fact that we employ a completely random site model to represent the defect fluorite structure, whereas the octahedrally coordinate sites may be further stabilized due to the transformation from the initial pyrochlore structure in the experiments. As such, we hypothesize that the splitting observed in the experimental EELS are a direct consequence of the larger fraction of octahedrally coordinated sites.

The oxygen conduction in ordered and disordered structures are estimated based on the atomic models of pyrochlore and defect fluorite structures which show a clear enhancement in the oxygen diffusivity in the Figure 6. The MD simulations were performed at 2000 K for 200 ps on the structures. The oxygen diffusion is captured via mean square displacement (MSD) of O atoms which is related to diffusivity (D) with the relationship, MSD = 6Dt, where t is time. The defect fluorite structure in $Gd_2Ti_xZr_{2-x}O_7$ (x = 0, 1, 2) exhibit high oxygen diffusivity evidenced by the

slope of the MSD curve as compare to the pyrochlore structures. The transition from ordered pyrochlore to disordered defect fluorite structure leads to the randomization of well-positioned oxygen vacancies and thus lowers the energy barrier for easier oxygen migration.[32-34] This suggests that the breaking the atomic ordering in the defect fluorite structure opens a pathway for easier oxygen diffusion.

CONCLUSIONS

In conclusion, we have revealed the effect of disorder on the correlation between electronic and atomic structure in $Gd_2Ti_2O_7$. With the aid of quantitative HAADF imaging, EELS, MD simulations and DFT calculations, the sub-angstrom scale insights on the role of disordering induced local atomic environment variations on the electronic structure. We demonstrated that local modification in oxygen coordination to the Ti cations resulted in dramatic changes in the crystal field splitting which defines the electronic structure. In particular, we showed that the reduction in octahedral coordination drives the transformation from a well-defined peak splitting in the pyrochlore phase to a broadened DOS in the amorphous structure. Interestingly, we find that theoretical predictions for a truly random defect fluorite structure predict peak shifts and broadening commensurate with the amorphous phase. A clear correlation between TiO_x polyhedra and electronic structure provides us with a fundamental understanding of the creation of disordered structures in $Gd_2Ti_2O_7$. With the help of theoretical atomic structure models, we estimated the dramatic enhancement in oxygen diffusivity in the defect fluorite structure as compared to ordered pyrochlore structured $Gd_2Ti_xZr_{2-x}O_7$ (x = 0, 1, 2). Through this work, we showed that the high-energy ion irradiation is a useful technique to engineer the atomically disordered nanochannels. These have fundamental consequences for the transport and probably an enhanced mobility of

oxygen ions within these nanochannels, thereby, providing a new route to tune materials for use in applications requiring fast ionic conduction.

Conflict of Interest

The authors declare no competing financial interest.

Supporting Information

Details of computed atomic structures and core-loss EELS spectra for O-K edge (pyrochlore, defect fluorite and amorphous). Supporting Information is available free of charge on ACS Publications website.

Acknowledgements

This research was supported by the U.S. Department of Energy, Office of Science, Basic Energy Sciences, Materials Science and Engineering Division. VRC was sponsored by the US Department of Energy (DOE), Office of Science, Basic Energy Sciences (BES), Materials Sciences and Engineering Division through the Office of Science Early Career Research Program. B.K.V. acknowledges summer support through the HERE program at ORNL. M.L. contribution was supported as part of the Materials Science of Actinides, an Energy Frontier Research Center funded by the U.S. Department of Energy, Office of Science, Basic Energy Sciences under Award # DE-SC0001089. This simulation used resources of the National Energy Research Scientific Computing Center, supported by the Office of Science, US Department of Energy, under Contract No. DEAC02-05CH11231.

REFERENCES

(1) Pennycook, T. J.; Beck, M. J.; Varga, K.; Varela, M.; Pennycook, S. J.; Pantelides, S. T. Origin of Colossal Ionic Conductivity in Oxide Multilayers: Interface Induced Sublattice Disorder. *Phys. Rev. Lett.* **2010**, *104*, 115901.

(2) Aidhy, D. S.; Sachan, R.; Zarkadoula, E.; Pakarinen, O.; Chisholm, M. F.; Zhang, Y.; Weber, W. J. Fast Ion Conductivity in Strained Defect-fluorite Structure Created by Ion Tracks in $Gd_2Ti_2O_7$. *Sci. Rep.* **2015**, *5*, 16297.

(3) Tuller, H., Ionic Conduction and Applications. In Springer Handbook of Electronic and Photonic Materials, Kasap, S.; Capper, P., Eds. Springer US: **2007**; pp 213-228.

(4) Tuller, H. L. Ionic Conduction in Nanocrystalline Materials. *Solid State Ionics* **2000**, *131*, 143-157.

(5) Moon, P. K.; Tuller, H. L. Ionic Conduction in the $Gd_2Ti_2O_7$–$Gd_2Zr_2O_7$ System. *Solid State Ionics* **1988,** *28*, 470-474.

(6) Tuller, H. L. Oxygen Ion Conduction and Structural Disorder in Conductive Oxides. *J. Phys. Chem. Solids* **1994**, *55*, 1393-1404.

(7) Takamura, H.; Tuller, H. L. Ionic Conductivity of Gd_2GaSbO_7–$Gd_2Zr_2O_7$ Solid Solutions with Structural Disorder. *Solid State Ionics* **2000**, *134*, 67-73.

(8) Diazguillen, J.; Diazguillen, M.; Padmasree, K.; Fuentes, A.; Santamaria, J.; Leon, C. High Ionic Conductivity in the Pyrochlore-type $Gd_{2-y}La_yZr_2O_7$ Solid Solution ($0 \leq y \leq 1$). *Solid State Ionics* **2008**, *179*, 2160-2164.

(9) Lian, J.; Wang, L. M.; Wang, S. X.; Chen, J.; Boatner, L. A.; Ewing, R. C. Nanoscale Manipulation of Pyrochlore: New Nanocomposite Ionic Conductors. *Phys. Rev. Lett*. **2001**, 87, 145901.

(10) Pirzada, M.; Grimes, R. W.; Minervini, L.; Maguire, J. F.; Sickafus, K. E. Oxygen Migration in $A_2B_2O_7$ Pyrochlores. *Solid State Ionics* **2001**, *140*, 201-208.

(11) Sachan, R.; Zarkadoula, E.; Lang, M.; Trautmann, C.; Zhang, Y.; Chisholm, M. F.; Weber, W. J. Insights on Dramatic Radial Fluctuations in Track Formation by Energetic Ions. *Sci. Rep.* **2016**, *6*, 27196.

(12) Wuensch, B. J.; Eberman, K. W.; Heremans, C.; Ku, E. M.; Onnerud, P.; Yeo, E. M. E.; Haile, S. M.; Stalick, J. K.; Jorgensen, J. D. Connection between Oxygen-ion Conductivity of Pyrochlore Fuel-cell Materials and Structural Change with Composition and Temperature. *Solid State Ionics* **2000**, *129*, 111-133.

(13) Sickafus, K. E.; Minervini, L.; Grimes, R. W.; Valdez, J. A.; Ishimaru, M.; Li, F.; McClellan, K. J.; Hartmann, T. Radiation Tolerance of Complex Oxides. *Science* **2000**, *289*, 748-751.

(14) Uberuaga, B. P. Complex oxides: Intricate Disorder. *Nat. Mater.* **2016**, *15*, 496-497.

(15) Chartier, A.; Catillon, G.; Crocombette, J.P. Key Role of the Cation Interstitial Structure in the Radiation Resistance of Pyrochlores. *Phys. Rev. Lett*. **2009**, *102*, 155503.

(16) Catillon, G.; Chartier, A., Pressure and temperature phase diagram of $Gd_2Ti_2O_7$ under irradiation. *J. Appl. Phys.* **2014**, *116*, 193502.

(17) Ewing, R. C. Nuclear Waste Disposal-pyrochlore ($A_2B_2O_7$): Nuclear Waste Form for the Immobilization of Plutonium and "Minor" Actinides. *J. Appl. Phys.* **2004**, *95*, 5949.

(18) Sickafus, K. E.; Grimes, R. W.; Valdez, J. A.; Cleave, A.; Tang, M.; Ishimaru, M.; Corish, S. M.; Stanek, C. R.; Uberuaga, B. P. Radiation-induced Amorphization Resistance and Radiation Tolerance in Structurally Related Oxides. *Nat. Mater.* **2007**, *6*, 217-23.

(19) Aluri, E. R.; Grosvenor, A. P. An Investigation of the Electronic Structure and Structural Stability of $RE_2Ti_2O_7$ by Glancing Angle and Total Electron Yield XANES. *J. Alloys Compd.* **2014**, *616*, 516-526.

(20) Shamblin, J.; Feygenson, M.; Neuefeind, J.; Tracy, C. L.; Zhang, F.; Finkeldei, S.; Bosbach, D.; Zhou, H.; Ewing, R. C.; Lang, M. Probing Disorder in Isometric Pyrochlore and Related Complex Oxides. *Nat. Mater.* **2016**, *15*, 507-511.

(21) Jozwik-Biala, I.; Jagielski, J.; Arey, B.; Kovarik, L.; Sattonnay, G.; Debelle, A.; Mylonas, S.; Monnet, I.; Thomé, L. Effect of Combined Local Variations in Elastic and Inelastic Energy Losses on the Morphology of Tracks in Ion-irradiated Materials. *Acta Mater.* **2013**, *61*, 4669-4675.

(22) Sachan, R.; Pakarinen, O. H.; Liu, P.; Patel, M. K.; Chisholm, M. F.; Zhang, Y.; Wang, X. L.; Weber, W. J. Structure and Band Gap Determination of Irradiation-induced Amorphous Nano-channels in $LiNbO_3$. *J. Appl. Phys.* **2015**, *117*, 135902.

(23) Kresse, G.; Joubert, D. From Ultrasoft Pseudopotentials to the Projector Augmented-wave Method. *Phys. Rev. B* **1999**, *59*, 1758-1775.

(24) Perdew, J. P.; Burke, K.; Ernzerhof, M. Generalized Gradient Approximation Made Simple. *Phys. Rev. Lett.* **1996**, *77*, 3865-3868.

(25) Toulemonde, M.; Assman, W.; Dufour, C.; Meftah, A.; Studer, F.; Trautmann, C. *Ion Beam Science: Solved and Unsolved Problems*. The Royal Danish Academy of Sciences and Letters: Copenhagen, Denmark; 2006.

(26) Lang, M.; Lian, J.; Zhang, J.; Zhang, F.; Weber, W. J.; Trautmann, C.; Ewing, R. C. Single-ion Tracks in $Gd_2Zr_{2-x}Ti_xO_7$ Pyrochlores Irradiated with Swift Heavy Ions. *Phys. Rev.* B **2009**, *79*, 224105.

(27) Gupta, S.; Gehrke, H. G.; Krauser, J.; Trautmann, C.; Severin, D.; Bender, M.; Rothard, H.; Hofsäss, H. Conducting Ion Tracks Generated by Charge-selected Swift Heavy Ions. *Nucl. Instrum. Methods Phys. Res., Sect. B* **2016**, *381*, 76-83.

(28) Lang, M.; Toulemonde, M.; Zhang, J.; Zhang, F.; Tracy, C. L.; Lian, J.; Wang, Z.; Weber, W. J.; Severin, D.; Bender, M.; Trautmann, C.; Ewing, R. C. Swift Heavy Ion Track Formation in $Gd_2Zr_{2-x}Ti_xO_7$ Pyrochlore: Effect of Electronic Energy Loss. *Nucl. Instrum. Methods Phys. Res., Sect. B* **2014**, *336*, 102-115.

(29) Liu, B.; Wang, J. Y.; Li, F. Z.; Zhou, Y. C. Theoretical Elastic Stiffness, Structural Stability and Thermal Conductivity of $La_2T_2O_7$ (T = Ge, Ti, Sn, Zr, Hf) Pyrochlore. *Acta Mater.* **2010**, *58*, 4369-4377.

(30) Zunger, A.; Wei, S. H.; Ferreira, L. G.; Bernard, J. E. Special Quasirandom Structures. *Phys. Rev. Lett.* **1990**, *65*, 353-356.

(31) Voas, B. K.; Usher, T.-M.; Liu, X.; Li, S.; Jones, J. L.; Tan, X.; Cooper, V. R.; Beckman, S. P. Special Quasirandom Structures to Study the $(K_{0.5}Na_{0.5})NbO_3$ Random Alloy. *Phys. Rev. B* **2014**, *90*, 024105.

(32) Wilde, P. J.; Catlow, C. R. A. Defects and Diffusion in Pyrochlore Structured Oxides. *Solid State Ionics* **1998**, *112*, 173-183.

(33) Wilde, P. J.; Catlow, C. R. A. Molecular Dynamics Study of the Effect of Doping and Disorder on Diffusion in Gadolinium Zirconate. *Solid State Ionics* **1998**, *112*, 185-195.

(34) Perriot, R.; Uberuaga, B. P. Structural vs. Intrinsic Carriers: Contrasting Effects of Cation Chemistry and Disorder on Ionic Conductivity in Pyrochlores. *J. Mater. Chem. A* **2015**, *3*, 11554-11565.

FIGURES

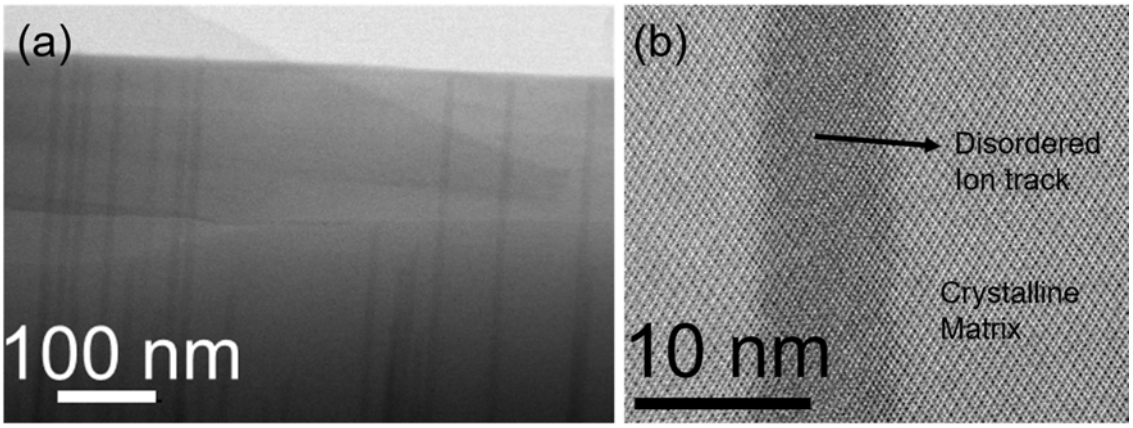

Figure 1. (a) An overview cross-section annular bright field (ABF) image of continuous nanochannels/ion tracks embedded in pyrochlore structured $Gd_2Ti_2O_7$. (b) Cross-sectional ABF image of an individual ion track showing the continuity of the disordered structure.

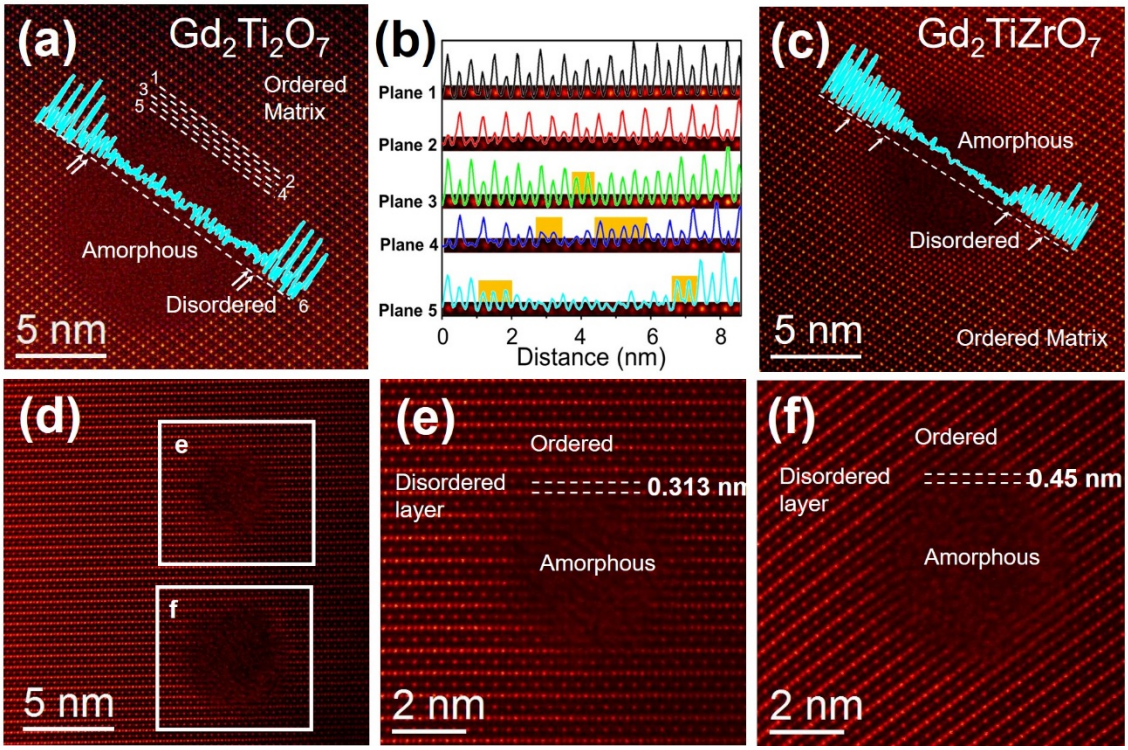

Figure 2. Thickness determination of defect fluorite shell around amorphous phase in an ion track. (a) Plan view HAADF image of track in (110) oriented $Gd_2Ti_2O_7$ matrix formed by 2.2 GeV Au ion. An atomic intensity profile is overlaid corresponding to the dotted line (marked as 6) exhibiting the defect fluorite phase at the periphery of amorphous track (indicated by arrows). (b) Intensity profile corresponding to plane 1-5 as shown in figure 2a. (c) Plan view ion track image of ion track in Gd_2TiZrO_7 matrix formed by 2.3 GeV Pb ion. (d-f) HAADF images of tracks formed by 55 MeV I ions exhibiting the formation of 3-5 Å thick disordered region.

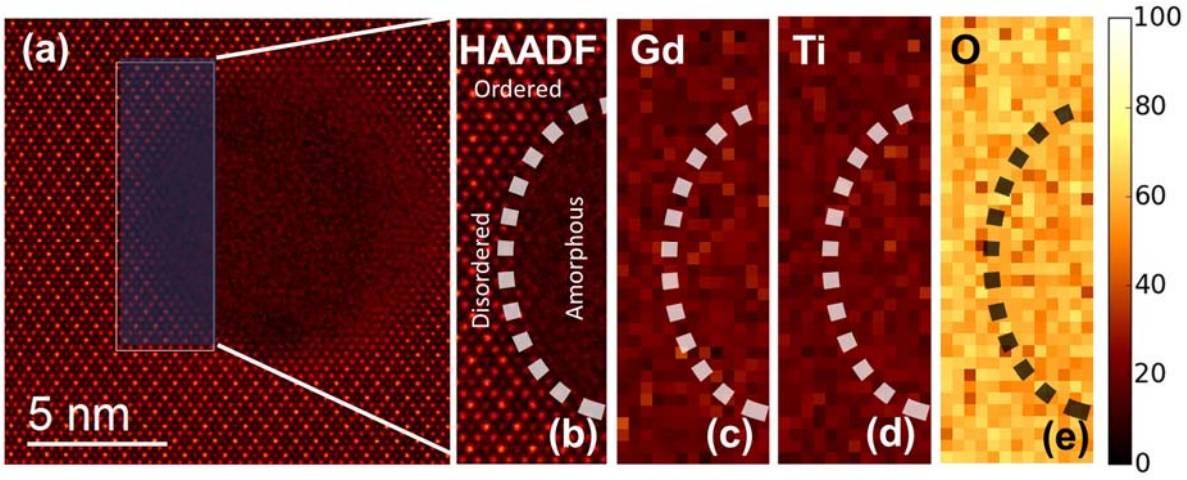

Figure 3. (a) A plan view HAADF image of an ion track in $Gd_2Ti_2O_7$. (b) Magnified HAADF image of the selected region in (a). EEL elemental map of (c) Gd, (d) Ti and (e) O corresponding to the region shown in (b). The region consists of amorphous, disordered defect fluorite and ordered pyrochlore matrix. The maps show that the average elemental composition the ion track is similar to the matrix within the measurement accuracy and suggest that no compositional changes took place during the process of track formation. Pixel size used for this data acquisition was 0.27 nm.

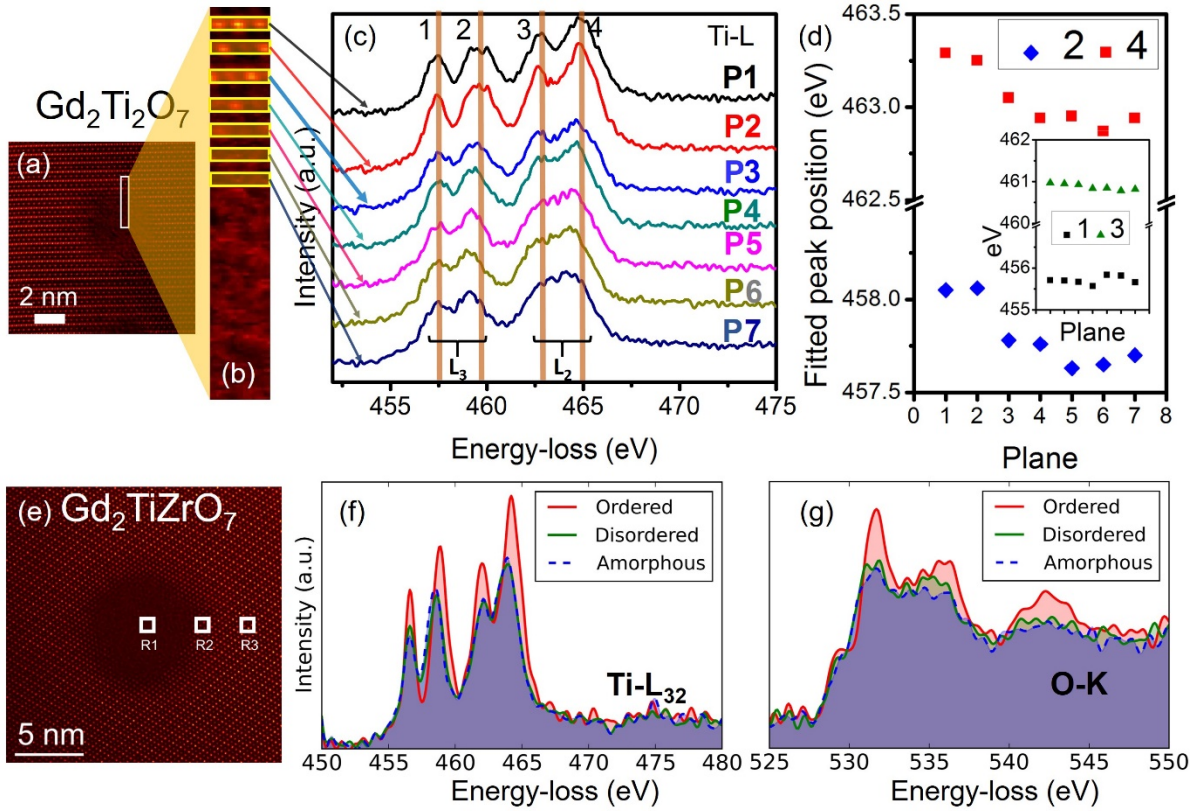

Figure 4. (a) A plan-view HAADF image of an ion track, earlier discussed in Figure 2e. (b) A magnified HAADF image of the marked region in (a), consisting of pyrochlore, defect fluorite and amorphous region. Various atomic planes are marked in the image over which EELS data was acquired. (c) Plane by plane Ti L_{23}-edge EEL spectra corresponding to the planes marked in (b). Plane 1-2, 3-4 and 5-7 correspond to pyrochlore, defect fluorite and amorphous respectively. (d) A plot showing the energy position of fitted peaks for plane 1-7. Figure shows a decrement in energy position of peak 2 and 4 between planes 2-3. The inset figure shows energy positions of peak 1 and 3 remain unchanged within the fitting deviation limits. (e) A plan-view HAADF image of ion track in Gd_2TiZrO_7. (f) Ti L_{23}-edge and (g) O K-edge EEL spectra corresponding to plane ordered, disordered and amorphous phases from regions marked in (e).

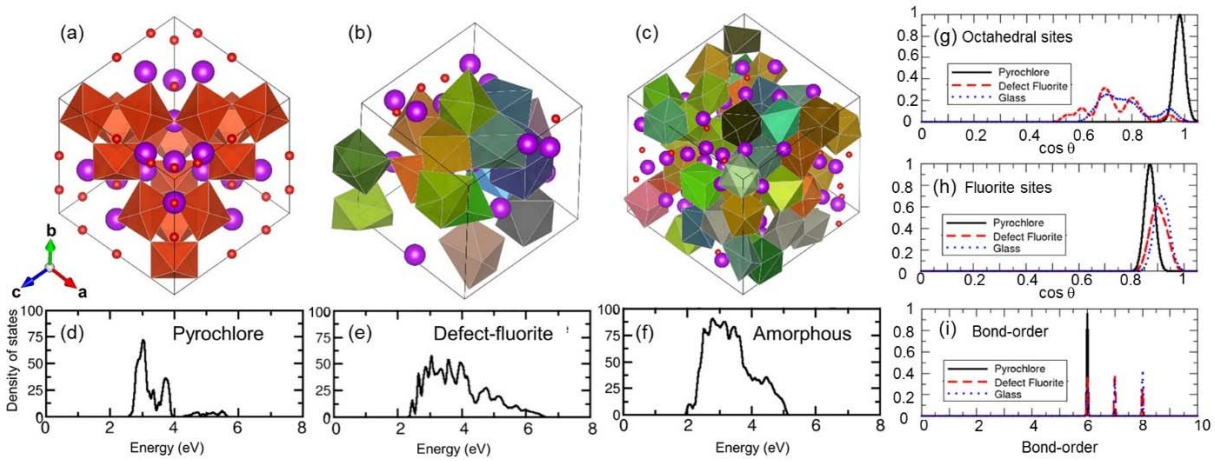

Figure 5. Atomic configuration of Ti-O polyhedra in (a) pyrochlore, (b) defect-fluorite and (c) amorphous structures. Ti-O octahedral are shown by red color in pyrochlore structure. In rest of atomic models, a range of color schemes are used to show the presence of various types of polyhedra. (d-f) The density of states in pyrochlore, defect fluorite and amorphous phase respectively, based on the shown atomic configurations. The O and Gd atoms are represented by red and violet colored balls. (g-h) The histograms illustrating the O-Ti-O angle deviation in polyhedra present in pyrochlore, defect-fluorite and amorphous atomic configurations with respect to ideal (g) octahedral sites and (h) Fluorite sites. (i) A distribution showing the variation in bond order present in aforementioned structures.

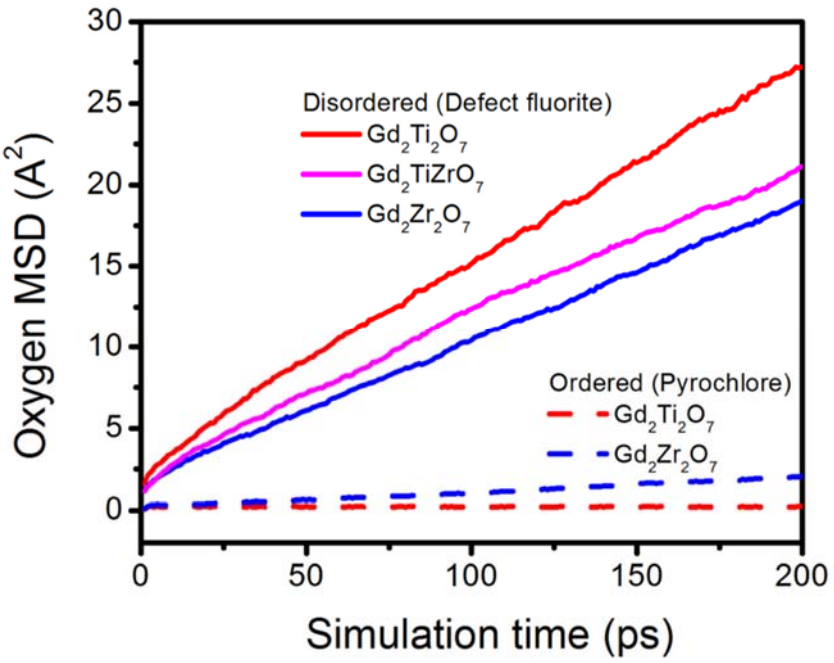

Figure 6. Mean square displacement (MSD) of oxygen in defect-fluorite and pyrochlore structure by MD simulations at 2000 K. Higher MSD slope in disordered defect fluorite than pyrochlore structure reveals higher oxygen diffusivity.

Figure 1. (a) An overview cross-section annular bright field (ABF) image of continuous nanochannels/ion tracks embedded in pyrochlore structured Gd2Ti2O7. (b) Cross-sectional ABF image of an individual ion track showing the continuity of the disordered structure.

Figure 2. Thickness determination of defect fluorite shell around amorphous phase in an ion track. (a) Plan view HAADF image of track in (110) oriented Gd2Ti2O7 matrix formed by 2.2 GeV Au ion. An atomic intensity profile is overlaid corresponding to the dotted line (marked as 6) exhibiting the defect fluorite phase at the periphery of amorphous track (indicated by arrows). (b) Intensity profile corresponding to plane 1-5 as shown in figure 2a. (c) Plan view ion track image of ion track in Gd2TiZrO7 matrix formed by 2.3 GeV Pb ion. (d-f) HAADF images of tracks formed by 55 MeV I ions exhibiting the formation of 3-5 Å thick disordered region.

Figure 3. (a) A plan view HAADF image of an ion track in Gd2Ti2O7. (b) Magnified HAADF image of the selected region in (a). EEL elemental map of (c) Gd, (d) Ti and (e) O corresponding to the region shown in (b). The region consists of amorphous, disordered defect fluorite and ordered pyrochlore matrix. The maps show that the average elemental composition the ion track is similar to the matrix within the measurement accuracy and suggest that no compositional changes took place during the process of track formation.

Figure 4. (a) A plan-view HAADF image of an ion track, earlier discussed in Figure 2e. (b) A magnified HAADF image of the marked region in (a), consisting of pyrochlore, defect fluorite and amorphous region. Various atomic planes are marked in the image over which EELS data was acquired. (c) Plane by plane Ti L23-edge EEL spectra corresponding to the planes marked in (b). Plane 1-2, 3-4 and 5-7 correspond to pyrochlore, defect fluorite and amorphous respectively. (d) A plot showing the energy position of fitted peaks for plane 1-7. Figure shows a decrement in energy position of peak 2 and 4 between planes 2-3. The inset figure shows energy positions of

peak 1 and 3 remain unchanged within the fitting deviation limits. (e) A plan-view HAADF image of ion track in Gd2TiZrO7. (f) Ti L23-edge and (g) O K-edge EEL spectra corresponding to plane ordered, disordered and amorphous phases from regions marked in (e).

Figure 5. Atomic configuration of Ti-O polyhedra in (a) pyrochlore, (b) defect-fluorite and (c) amorphous structures. Ti-O octahedral are shown by red color in pyrochlore structure. In rest of atomic models, a range of color schemes are used to show the presence of various types of polyhedra. (d-f) The density of states in pyrochlore, defect fluorite and amorphous phase respectively, based on the shown atomic configurations. The O and Gd atoms are represented by red and violet colored balls. (g-h) The histograms illustrating the O-Ti-O angle deviation in polyhedra present in pyrochlore, defect-fluorite and amorphous atomic configurations with respect to ideal (g) octahedral sites and (h) Fluorite sites. (i) A distribution showing the variation in bond order present in aforementioned structures.

Figure 6. Mean square displacement (MSD) of oxygen in defect-fluorite and pyrochlore structure by MD simulations at 2000 K. Higher MSD slope in disordered defect fluorite than pyrochlore structure reveals higher oxygen diffusivity.

TOC Graphic